Number size distribution and charging properties of sub-10 nm metal-based particles produced by spark ablation at atmospheric pressure

Liu, Yiliang; Attoui, Michel; Baalbaki, Rima; Cai, Runlong; Biskos, George; Chen, Yang; Kangasluoma, Juha

DOI
10.1080/02786826.2024.2355174

Publication date
2024

Document Version
Final published version

Published in
Aerosol Science and Technology

Citation (APA)
Liu, Y., Attoui, M., Baalbaki, R., Cai, R., Biskos, G., Chen, Y., & Kangasluoma, J. (2024). Number size distribution and charging properties of sub-10 nm metal-based particles produced by spark ablation at atmospheric pressure. *Aerosol Science and Technology*, *58*(8), 902-914. https://doi.org/10.1080/02786826.2024.2355174

Aerosol Science and Technology

ISSN: (Print) (Online) Journal homepage: www.tandfonline.com/journals/uast20

Number size distribution and charging properties of sub-10 nm metal-based particles produced by spark ablation at atmospheric pressure

Yiliang Liu, Michel Attoui, Rima Baalbaki, Runlong Cai, George Biskos, Yang Chen & Juha Kangasluoma

To cite this article: Yiliang Liu, Michel Attoui, Rima Baalbaki, Runlong Cai, George Biskos, Yang Chen & Juha Kangasluoma (05 Jun 2024): Number size distribution and charging properties of sub-10 nm metal-based particles produced by spark ablation at atmospheric pressure, Aerosol Science and Technology, DOI: 10.1080/02786826.2024.2355174

To link to this article: https://doi.org/10.1080/02786826.2024.2355174

AEROSOL SCIENCE AND TECHNOLOGY
https://doi.org/10.1080/02786826.2024.2355174

Number size distribution and charging properties of sub-10 nm metal-based particles produced by spark ablation at atmospheric pressure

Yiliang Liu[a,b,c], Michel Attoui[d], Rima Baalbaki[a], Runlong Cai[a], George Biskos[e,f], Yang Chen[b,c], and Juha Kangasluoma[a]

[a]Institute for Atmospheric and Earth System Research/Physics, University of Helsinki, Helsinki, Finland; [b]Research Center for Atmospheric Environment, Chongqing Institute of Green and Intelligent Technology, Chinese Academy of Sciences, Chongqing, P. R. China; [c]College of Resources and Environment, Chongqing School, University of Chinese Academy of Sciences, Chongqing, P. R. China; [d]LISA, UMR7583, Université Paris-Est-Créteil, Université de Paris, Institut Pierre Simon Laplace (IPSL), Créteil, France; [e]Climate and Atmosphere Research Center, The Cyprus Institute, Nicosia, Cyprus; [f]Faculty of Civil Engineering and Geosciences, Delft University of Technology, Delft, Netherlands

ABSTRACT

Sub-10 nm metal-based nanoparticles have garnered immense interest due to their unique properties and versatile applications. In this study, we created sub-10 nm Ag-based particles with a spark discharge generator and explored the parameters impacting their size distribution and charging properties, including carrier gas flow rates, spark discharge voltage, electrode gap distances, and capacitance. Our findings illuminate that there is a comparable influence of different factors on both self-charged and neutral particles. Among the different factors, carrier gas flow rates emerging as a paramount determinant in particle size. While increasing spark discharge voltage and capacitance within the spark circuit increases particle concentrations, the associated changes in particle size prove to be less straightforward. Significant differences between the concentration of positive and negative self-charged particles manifest when the carrier gas flow rate surpasses 5.0 L min^{-1}, with positive particles ranging from 0.8 to 1.2 nm and negative particles spanning 0.8 to 3.0 nm. Self-charged particles close to 1 nm tend to exhibit positive charges, whereas those larger than 2 nm tend to acquire negative charges, which suggests the growth of negative particles is faster than positive ones in the spark chamber. Nevertheless, these disparities between bipolar particles diminish with the increase of residence time, leading to the observation of similar particle size distributions. Positive particles consistently bear a single charge, while some negative particles exceeding 3 nm exhibit multiple charges, primarily under carrier gas flow rates exceeding 7.5 L min^{-1}. This study provides insights into the control of properties of nano-sized metal particles, which are crucial for their practical utilization.

ARTICLE HISTORY
Received 9 December 2023
Accepted 30 April 2024

EDITOR
Jim Smith

1. Introduction

Nano-sized metal particles exhibit distinct properties and reactivity that render them highly valuable across diverse application domains, such as catalysis, nanomaterials, biomedicine, optics, photonics, and energy conversion/storage (Han et al. 2022; Zhu, Jin, and Sun 2011; Kimble et al. 2004; Boyen et al. 2002). The distinctive characteristics and behaviors of the metal particles are linked to their sizes and compositions. Particularly within the nano-size range, metal particles exhibit non-scalable traits in terms of ionization potential, thermodynamics, and catalytic activity (Luo, Castleman, and Khanna 2016). The synthesis of metal nanoparticles with a controlled size and specific composition holds crucial importance.

A series of techniques are employed to synthesize nano-sized metal particles, encompassing chemical synthesis, physical vapor deposition, laser ablation, electrochemical methods, etc. (Ahmed and Kostko 2020; Smalley 1983). Wet chemistry method is widely used in laboratory for metal particle synthesis. However, this method requires the use of solvents and surfactants, and thereby is hindered by low production rates and contamination, which further limits its industrial applicability. Gas-phase methods offer more versatile and environmentally friendly alternatives. Laser ablation can directly and locally vaporize bulk materials to

CONTACT Yang Chen chenyang@cigit.ac.cn Chongqing Institute of Green and Intelligent Technology, Chinese Academy of Science, 266 Fangzheng Ave., Beibei Dist., Chongqing, 400714, P. R. China.

Supplemental data for this article can be accessed online at https://doi.org/10.1080/02786826.2024.2355174.

form nanoparticles, and thereby offers elevated purity and nanoparticle concentrations (Morales and Lieber 1998). However, the high operation cost and the potential security risk with high-power lasers remain a barrier for broad industrial application. By comparison, spark ablation is an effective technique for preparing metal particle (Schwyn, Garwin, and Schmidt-Ott 1988). Spark discharge generator produce metal-based particles in a simple, inexpensive, and environmentally friendly manner as it does not require chemical precursors (Wondergem et al. 2020; Domaschke, Lübbert, and Peukert 2019; Isaac et al. 2016; Kim and Chang 2005). The size distribution as well as the corresponding composition of metal particles are measured in some previous studies by using a DMA-MS system, suggesting the presence of atomic clusters at the smallest sizes (Maisser et al. 2015, 2021). Notably, precise control over the nucleation process enables the creation of nano-sized particles with high purity, achieved by carefully managing the behavior of nanoparticles prior to their deposition and immobilization (Petallidou et al. 2023; Pfeiffer, Feng, and Schmidt-Ott 2014; Tabrizi et al. 2008).

A recently published book gives an overview of the development of spark ablation, as well as explains the principles of immobilizing particles to create novel nanoparticles (Spark Ablation, Building Blocks for Nanotechnology 2019). Extensive research has focused on elucidating the variables influencing the particle formation process by spark ablation (Feng, Biskos, and Schmidt-Ott 2015; Evans, Harrison, and Ayres 2003). The method can produce either spherical singlet nanoparticles having sizes smaller than ca. 10 nm depending on the material, or larger agglomerated structures. Distinct metals can lead to diverse particle sizes and morphologies, owing to variations in their thermodynamic properties and reactivity throughout the spark discharge process. The comprehensive effects of various factors on the formation of sub-100 nm particles have been detailed in a good review paper (Meuller et al. 2012). Briefly, the gas environment in which the spark discharge transpires assumes a pivotal role, with the composition and pressure of the surrounding gas wielding a significant influence on the kinetics of particle nucleation and growth. The flow rate of the carrier gas exerts an influence on the size distribution of the generated nanoparticles. Lower flow rates tend to yield a broader size distribution with a larger mean diameter (Scheibel and Porstendörfer 1983). The energy of each spark discharge is influenced by the electrode gap distance, carrier gas species and the corresponding pressure. The increase in spark energy would increase the metal production rate (Maisser et al. 2015), and thereby exhibited a direct correlation with particle size. With increasing capacitance, the particle size distribution shifts toward larger particle sizes (Ternero et al. 2023; Tabrizi et al. 2008).

Despite the great efforts, our understanding of the factors affecting the formation of sub-10 nm metal-based particles remains elusive, primarily due to lack of composition measurements that would reveal the step growth of metal particles. Moreover, the charging properties of sub-10 nm particles produced *via* the spark discharge generator remain unclear. In the limited researches, some conflicting findings are worth noting. Tabrizi et al. conducted a study in which they examined the size distribution of metal particles measuring below 30 nm, both in the presence and absence of a neutralizer. Their findings concluded that as much as 20% of these particles retained a negative charge, deviating significantly from the expected bipolar charging state (Tabrizi et al. 2008). On the other hand, Bau et al. conducted an investigation focusing on copper, aluminum, and graphite particles generated by a commercial spark discharge generator (Bau et al. 2010). Their research indicated that nearly 100% of sub-10 nm particles remained neutral. Lack of a comprehensive understanding of charging characteristics sets constraints on the precise selection of metal particles based on their electrical mobility. For instance, when the charge fraction of metal particles is exceedingly low, it is advisable to consider the use of a neutralizer, whereas in different scenarios, its application may be deemed unnecessary. Furthermore, the presence of multiply charged particles needs to be investigated, as it also has an impact on the accuracy of particle classification based on electrical mobilities.

In this study, we measure the size distribution of both self-charged particles and total particles, respectively. Self-charged particles refer to those particles acquiring charge within the spark discharge generator, without the use of a neutralizer. We investigate the effects of different factors on particle size distributions and delve into the charging properties of sub-10 nm particles, including multiple charging conditions and size-resolved charge fractions.

2. Methods

2.1. Working principles of the spark discharge generator

The spark discharge generator employed in this study consists of a stainless-steel chamber. The chamber encloses two opposing cylindrical electrodes crafted

from pure silver, each with a diameter of 2 mm. The distance between these electrodes can be adjusted, ranging from 0 to several millimeters. While one electrode connects to a high voltage power supply (HVPS, Technix Inc., France) enabling spark discharge voltages (V_d) within the range of −10 to 10 kV, the other electrode remains grounded. When the applied voltage surpasses the breakdown threshold, it triggers a high-energy electrical discharge between the electrodes, forming a conducting channel. Control of electrical emission for each spark is achieved through a capacitor in the circuit, offering adjustable capacitance (C) within the range of 1 to 6 nF. As either the capacitance or spark discharge voltage increases, so does the energy transferred per spark discharge (E). This energy within each spark is given by the energy stored in the capacitor according to the Equation:

$$E = \frac{CV_d^2}{2} \quad (1)$$

Under the influence of electric field forces, bipolar ions accelerate, attaining high energy levels before colliding with the electrode surfaces. The intense heat, pressure, and electric field generated during the discharge cause the vaporization of the electrode material. The mass production rate of metal vapors (m) is given by Tabrizi et al. (2008):

$$m = A(E - E_0)f \quad (2)$$

where A represents a material-dependent constant, E stands for spark energy, E_0 denotes the minimum energy required for particle generation, and f signifies the spark repetition frequency. High-purity nitrogen serves as the carrier gas, with a flow rate adjustable between 2.5 to 12.5 L min^{-1}. The carrier gas rapidly quenches the metal vapors, inducing supersaturation (Tabrizi et al. 2008). The growth governed by condensation and particle-particle collisional growth can be considered to start from the atomic scale (Feng, Biskos, and Schmidt-Ott 2015).

2.2. Instrument setup

As displayed in Figure 1, three experiments were performed, with the experiment conditions being summarized in Table 1. We cleaned the spark discharge generator thoroughly before experiment, while the high-purity nitrogen (purity > 99.999%) was used as the carrier without further purification, because we think this is a commonly accepted cleanness under the laboratory conditions.

In the first experiment, nanoparticles produced by the spark discharge generator were directed into a half-mini Differential Mobility Analyzer (half-mini DMA, SEADM Inc., Spain) (Fernández de la Mora and Kozlowski 2013). The half-mini DMA operates consistently with a fixed sheath flow rate of ∼300 L min^{-1}. The half-mini DMA was calibrated by electrospraying a tetraheptylammonium cation methanol solution, achieving a resolution of 21 at 1.47 nm. The shortest possible tube (less than 5 cm) was employed between the spark discharge generator and the DMA inlet in order to minimize particle losses. Thereby, effective volume corresponding to coagulation (V_{eff}) was minimized and the metal-based particles at their

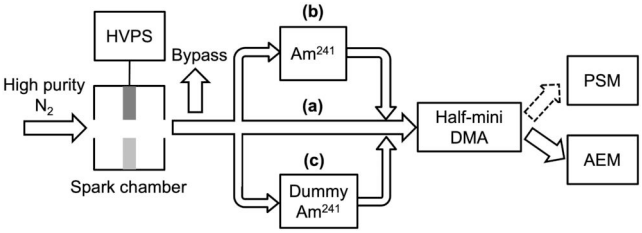

Figure 1. Schematic diagrams of the instrument setup for measuring the number size distributions of particles generated in the spark discharge generator. In the first experiment (a), the size distributions of self-charged particles are measured by connecting the spark chamber outlet with the DMA inlet directly. In the second experiment (b), total particles, which include both neutral and charged particles, are measured by incorporating an americium neutralizer (Am^{241}). In the third experiment (c), the size distributions of self-charged particles are measured by replacing the Am^{241} neutralizer with a dummy neutralizer. The diffusion losses are identical in the second and third experiments.

Table 1. A summary of experiments that have been performed.

No.	Neutralizer	Dummy neutralizer	Carrier gas	Flow rate (L min^{-1})	Flow rate through the neutralizer (L min^{-1})	High voltage (kV)	High voltage polarity	Capacitance (nF)	Gap distance (mm)
1			N_2	2.5; 5.0; 7.5; 10.0; 12.5	5.0; 2.5	6.5; 7.5; 8.5; 9.5	+/-	2.2; 4.4; 5.1	0.25; 0.50; 0.75
2	√		N_2	2.5; 5.0; 7.5; 10.0	5.0; 2.5	6.0; 7.0; 8.0; 9.0	+	3.0; 4.0; 4.4; 5.1	0.25; 0.50; 0.75
3		√	N_2	5.0; 7.5; 10.0; 12.5	5.0	6.0; 7.0; 8.0; 9.0	+/-	4.4	0.50

first formation stage were measured. The DMA outlet was linked to particle number concentration detectors, including an aerosol electrometer (AEM, Model 3068B, TSI Inc., USA) and a particle size magnifier (PSM, Airmodus Inc., Finland), to measure the size distributions (Cai et al. 2018; Vanhanen et al. 2011). When both the PSM and AEM detectors were utilized, the DMA sampling flow rate is maintained at 5.0 L min^{-1}, with each detector operating at 2.5 L min^{-1}. When the carrier gas flow rate was 2.5 L min^{-1}, only one detector, AEM, was utilized. Various factors affecting the size distribution were investigated, including the carrier gas flow rate (Q), spark discharge voltage (V_d), electrode gap distance, and capacitance (C) in the circuit.

In the second experiment, an americium neutralizer (Am^{241}, 60 MBq) was introduced to help the particles achieve charging steady-state (Wiedensohler 1988), allowing measurement of the number size distributions of total particles (including charged and neutral ones). Some high carrier gas rates were employed to investigate particles during their initial formation. However, the sample flow rate passing through the neutralizer was carefully controlled below 5.0 L min^{-1}, ensuring sufficient residence time to achieve a charging steady-state.

The third experiment replaced the Am^{241} with a dummy neutralizer. The role of this dummy neutralizer was to subject metal particles to equivalent diffusion losses as encountered in the second experiment. The charging state of self-charged particles is investigated by comparing it with the results displayed in the second experiment. Note that the addition of a neutralizer or a dummy could potentially cause some variation in size distribution because of diffusion losses and coagulation growth.

2.3. Data inversion

The size-resolved concentrations ($dN/dlogd_p$) of self-charged particles were inverted using a linear method outlined in previous studies (Equation (3)), which assumes constant particle size distribution and particle properties within the non-zero range of the DMA transfer function (Jiang et al. 2011; Stolzenburg and McMurry 2008).

$$\left.\frac{dN}{dlnd_p}\right|_{d_p^*} = \frac{N\ a^*}{\frac{Q_a}{Q_s}(1+\delta)f_c\left(d_p^*\right)\ \eta_{pene}\left(d_p^*\right)} \quad (3)$$

where N is the measured aerosol concentration by the AEM; d_p is the particle diameter; d_p* is the diameter of a particle with the electrical mobility equal to half-mini DMA transfer function centroid electrical mobility; a* is equal to the negative of the derivative of the natural logarithm of electrical mobility (Z_p) with respect to the natural logarithm of d_p, evaluated at d_p*, and a* has a value equal to 2 in this study; $f_c(d_p^*)$ is the fraction of charged particles; η_{pene} (d_p*) is the product of particle penetration efficiencies through the sampling lines and the half-mini DMA. The penetration efficiency across the half-mini DMA provided in a previous study was applied (Cai et al. 2018). For the measurement of the size distribution of self-charged particles, $f_c(d_p^*)$ has a value of 1. The particle size distribution of total particles, encompassing both charged and neutral entities, was inverted based on the assumption that nanoparticles reached a charging steady-state in the neutralizer. Nanoparticle production exhibits excellent repeatability over a span of 40 min (Figure S1). Consequently, all the results presented in the subsequent chapters stem from a single scan. The minor fluctuations in particle concentration can be attributed to inherent AEM noise and natural variations in particle concentrations.

Multiply charged particles refer to particles bearing more than one charge. Traditionally, the multiple charging has been characterized using methods such as tandem DMA system. However, this method is problematic when sub-10 nm particles present in low concentrations. In our study, the presence of multiply charged particles is explored through the calculation of ratios between concentrations obtained by the PSM (C_{PSM}) and the AEM (C_{AEM}) as:

$$ratio = \frac{C_{PSM}}{C_{AEM}} \quad (4)$$

Due to variations in their operational principles, the AEM and PSM exhibit distinct responses when confronted with multiply charged particles. In particular, the AEM operates under the assumption of one charge per particle, leading to an overestimation of particle concentration when multiply charged particles are present. Conversely, the PSM, unlike the AEM, does not overestimate the concentration of multiply charged particles. Considering that, we conducted measurements of the ratios between self-charged particles and compared them to those of singly charged particles after the introduction of a neutralizer. To avoid the influence of AEM background noise, only the AEM concentrations larger than 500 cm^{-3} are used for calculation. Ratio values for self-charged particles that exhibit a noticeable decrease compared to singly charged particles indicates the presence of multiple charging.

Based on Equation (5), the charge fraction of self-charged particles is computed subsequent to acquiring concentrations of size-resolved concentrations of both

self-charged particles ($conc_{self\text{-}charged}$) and total particles ($conc_{total}$). $Conc_{self\text{-}charged}$ (comprising both charged and neutral particles) is calculated using the results obtained with a dummy neutralizer, while $conc_{total}$ is calculated using Equation (3), based on the results obtained in the presence of a neutralizer. In the case of $conc_{total}$, both charged and neutral particles are accounted.

$$charge\ fraction = \frac{conc_{self-charged}}{conc_{total}} \quad (5)$$

In addition, the measurement uncertainties of PSM and AEM are calculated. Regarding the counting uncertainties of PSM, the Poisson counting uncertainty, represented by $\sqrt{N}$, signifies the standard deviation (σ) of the counted. Consequently, the counting uncertainties of concentrations measured by PSM can be expressed as $1/\sqrt{N}$ (Kangasluoma and Kontkanen 2017). As for the counting uncertainties of the Aerosol Electrometer (AEM), they mainly stem from instrument noise. Prior to each experimental group, the instrument's zero point is meticulously calibrated. Here, we have cited the values provided in the manual, indicating that the root mean square of the current signal at 1 s is less than 1 fA. Specifically, the uncertainties in Equations (4) and (5) are the sums of the counting uncertainties from PSM and AEM.

3. Results

3.1. Number size distribution of the self-charged particles

3.1.1. Effects of carrier gas flow rate

According a previous study that is performed with a similar particle generator and comparable operating conditions (Maisser et al. 2021), metal-based particles overwhelmingly dominated the mass spectrum. Trace impurities of water and oxygen that are present in the carrier gas exhibit a size- and polarity- dependent toward the metallic cluster. As a result, we regard all the particles measured in this study as metal-based particles.

In the first experiment, the size distributions of self-charged particles were examined across various carrier gas flow rates (Q) as illustrated in Figure 2. The effective volume corresponding to the transit of carrier gas from the electrode gap to the half-mini DMA inlet was approximately 2.45 cm^{-3}. Consequently, the residence time (V_{eff}/Q) between the initial generation of metal-based particles and their detection within the half-mini DMA equated to 59, 29, 20, 15, and 12 ms, under carrier gas flow rates of 2.5, 5.0, 7.5, 10.0, and 12.5 L min^{-1}, respectively. The spark frequency remained consistent across varying carrier gas flow rates, standing at 11 Hz in the experimental configuration. Each spark carried energy of ~178 mJ. While the mass production rate (Equation (2)) of metal vapors remained relatively stable, the metal mass per unit volume decreased proportionally as the carrier gas flow rate increased.

The extended residence time translated to a longer period for coagulation growth. As a result, both positive and negative self-charged particles were observed to shift toward larger sizes with decreasing carrier gas flow rate. This result is qualitatively consistent with the coagulation growth model (Equation (6)) (Feng, Biskos, and Schmidt-Ott 2015), for calculating particle size (d_p):

$$d_p = \left(\frac{3\beta V_{eff}\dot{m}}{\rho\pi Q^2}\right)^{1/3} \quad (6)$$

Where β is the coagulation kernel, evolving with time based on the momentary particle size distribution, temperature, gas flow conditions, and inter-particle forces.

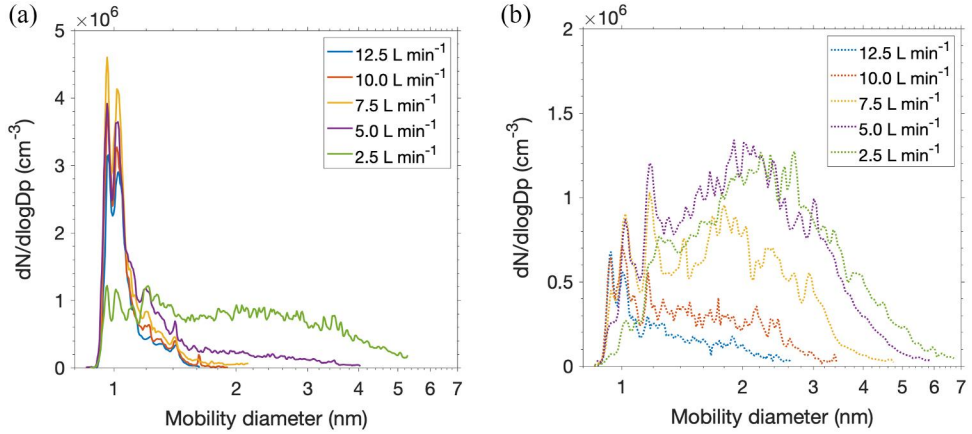

Figure 2. Effects of carrier gas flow rate on the size distribution of the self-charged particles. The experiments were conducted under the condition when the spark discharge voltage of +9 kV, electrode gap distance of 0.5 mm, and a capacitance of 4.4 nF. (a) The solid lines represent the results of self-charged positive particles. (b) Dashed lines represent the results of self-charged negative particles.

V_{eff} represents the effective volume incorporating the majority of the flow and engaged by coagulating aerosol, while ρ denotes material density. This expression serves to determine particle size as a function of gas flow rate (Q) and particle mass production rate ($\dot{m}$).

Significant distinctions manifest within the size distribution of self-charged positive and negative particles. For positive particles, when the carrier gas flow rate surpasses 5.0 L min^{-1}, particles are distributed within a narrow size range of 0.8–1.2 nm. As the carrier gas flow rate diminishes from 12.5 to 5.0 L min^{-1}, a marginal shift of particles toward larger sizes is observed. Meanwhile, two peaks at 0.96 and 1.02 nm are observed, with the concentrations undergoing an initial increase followed by a decline. When the carrier gas flow rate is further reduced to 2.5 L min^{-1}, the particle size distributions notably broaden, encompassing a wider spectrum of 0.9–6.0 nm. The increase in both residence time and mass production would promote the formation of larger sized particles through coagulation growth. For self-charged negative particles, a similar trend was observed, i.e., a shift toward larger particle sizes as the carrier gas flow rate decreased. However, the particle size distribution exhibited distinct characteristics compared to the positive particles. Instead of exhibiting prominent peaks around 1 nm, negative nanoparticles were dispersed across a wider size range. When the carrier gas flow rates vary between 5.0 and 10.0 L min^{-1}, a significant concentration of particles in the 2–3 nm size range becomes evident.

The reduction of the carrier gas flow rate resulted in the emergence of larger particles accompanied by a simultaneous increase in concentration. The total concentrations of self-charged particles are calculated. The positive particles exhibit a progressive decrease in concentration of 5.3, 3.8, 3.1, 2.5, and 2.1×10^5 cm^{-3}, respectively, as the flow rate escalates from 2.5 to 12.5 L min^{-1}. The total concentrations of self-charged negative particles follow a similar trend with the variation in carrier gas flow rates, registering values of 5.5, 5.7, 3.6, 1.6, and 0.9×10^5 cm^{-3}. At a carrier gas flow rate between 2.5 and 7.5 L min^{-1}, the total concentrations of negative particles slightly surpass those of positive ones. Conversely, at flow rates between 10.0 and 12.5 L min^{-1}, the concentrations of positive particles are significantly higher than negative particles. The mean diameters of both positive and negative particles are presented in Table 2. As the carrier gas flow rate decreases from 12.5 to 2.5 L min^{-1}, negative particles exhibit a larger diameter compared to positive particles. However, at the carrier gas flow rate of 2.5 L min^{-1}, the difference between the particle diameters becomes less significant. Additionally, prediction diameters based on Equation (6) are provided. These parameters are sourced from a previous study (Feng, Biskos, and Schmidt-Ott 2015), and the mobility diameters presented here are approximately 0.3 nm larger than the physical diameter predicted by Equation (6). Overall, the calculated results demonstrate a good correlation with the measured results when the carrier gas flow rate is between 5.0 and 10.0 L min^{-1}, with the predicted diameter falling between the measured sizes of positive and negative particles. At lower carrier gas flow rate of 2.5 L min^{-1}, the predicted diameter slightly exceeds the measured size of negative particles.

Table 2. Mean diameters of positive and negative particles with predicted diameters using Equation (6).

Carrier gas flow rate (L min^{-1})	2.5	5.0	7.5	10.0	12.5
Positive particle average diameter (nm)	2.14	1.31	1.09	1.08	1.07
Negative particle average diameter (nm)	2.44	2.12	1.87	1.56	1.33
Predicted diameter (nm)	2.52	1.70	1.37	1.18	1.06

All the diameters displayed here are mobility diameters. The experiments were conducted under the condition when the spark discharges voltage of +9 kV, electrode gap distance of 0.5 mm, and a capacitance of 4.4 nF.

Comparing the size-resolved concentrations, as well as the total concentrations of bipolar particles, we note that the disparities between positively and negatively charged particles are dependent on carrier gas flow rate. At a carrier gas flow rate of 2.5 L min^{-1}, comparable size distributions are observed between positive and negative particles. When the carrier gas flow rate exceeds 5.0 L min^{-1}, particles close to 1 nm exhibit significantly higher concentrations of positively charged particles than negatively charged ones. The opposite holds true for particles larger than 2 nm. The heightened carrier gas flow rate acts to rapidly dilute and restrain the coagulation growth of initially formed particles, leading to results that mirror the size distribution of Ag particles after their very first formation.

Although the exact composition of nanoparticles remains unmeasured in this study, insights from a previous investigation shed light on this matter (Maisser et al. 2021). In that study, it was observed that pure Ag and low oxidation state silver oxides tended to carry positive charges, while the silver oxides with relatively higher oxidation states, influenced by trace amounts of oxygen and/or water within the carrier gas, tended to be negatively charged. Our observation that the negatively charged particles are larger compared to their positively charged counterparts implies that their growth is faster, possibly due to the higher reactivity of negative

clusters with the surrounding molecules (Maisser et al. 2021).

An electric field forms between the high voltage electrode and the generator chamber, and direction of the electric field is determined by the voltage polarity. The electric field has the potential to induce different electrical losses between positive and negative particles. To investigate that, we manipulated the spark discharge voltage, transitioning it from positive to negative polarity. Notably, the size distributions (as depicted in Figure S2) show comparable pattern as those observed in Figure 2: self-charged positive particles exhibited a narrow size distribution, while negatively charged particles spanned a broader size spectrum. Consequently, the difference in size distributions between positive and negative particles cannot be attributed to electrical losses.

3.1.2. Effects of other factors

According to the Paschen's law, the break down voltage (V_b) for triggering the spark discharge between two electrodes in our setup is 3.7 kV. The spark discharge voltage (V_d) should be higher than the V_b. As depicted in Figure 3a, the influence of spark discharge voltage on the size distribution of self-charged positive particles is illustrated. With the increasing of discharge voltage from 6.5 to 9.5 kV, a noticeable increase in concentrations becomes evident (Figure 3a). Similar outcomes manifest when the capacitance (C) is increased from 2.2 to 5.1 nF (Figure 3b). Equations (1) and (2) shows that the mass production rate of metal vapors experiences a marked boost with the increase in spark energy. Nonetheless, the influence of the mass production rate on particle size remains moderate due to the cube root dependency in Equation (6).

With the gap distance between the two electrodes set to 0.25 mm, the generated particles exhibit lower concentrations and smaller sizes. However, as the gap distance extends further from 0.50 to 0.75 mm, a slight decline in particle concentrations becomes noticeable. In the context of our experimental setup, a gap distance of 0.50 mm emerges as the recommended setting for optimal metal particle production.

3.2. Number size distribution of the total particles

We then measured the number size distributions of total particles following the introduction of a neutralizer. This method led to the loss of size distribution information for metal-based particles close to 1 nm due to the overlapping size of neutralizer ions with the nano-sized metal particles. Specifically, positive neutralizer ions (without spark particles) were found to span the size range of 1.1–1.7 nm, whereas negative ions exhibited a size range of 0.9–1.4 nm (Figure S3). Thereby, the number size distributions of the total particles in the size range of 1.4–7.0 nm are inverted based on the particles that get negatively charged in the neutralizer.

Under identical particle generation conditions, the particle sizes of the total particles (as displayed in Figure 4a) exceed those of the self-charged particles (as displayed in Figure 2a). The increase in particle size can be attributed to the introduction of the neutralizer, which extended the residence time of metal-based particles before the measurement with the half-mini DMA. Similarly, an increase in particle size was also observed, when a dummy neutralizer was introduced in the sampling line (Figure S4). The influence of various factors on the size distributions of total particles

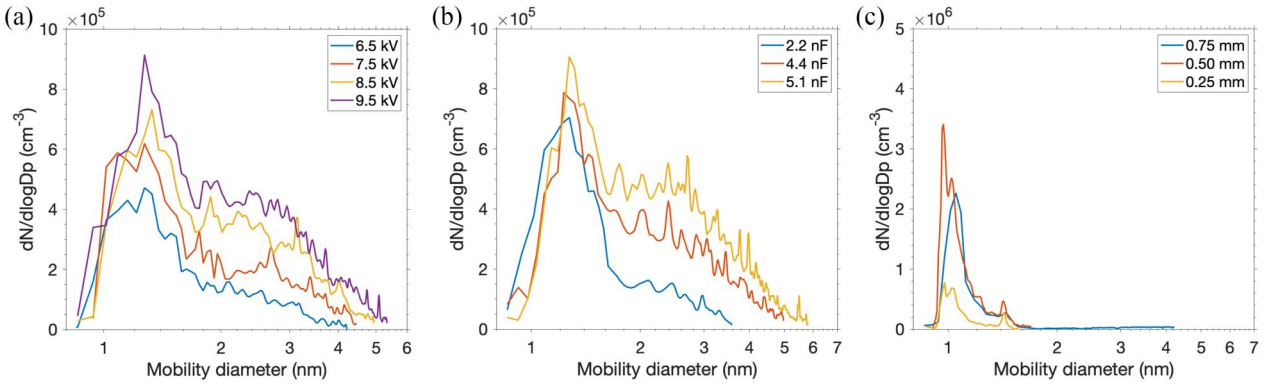

Figure 3. (a) Effects of spark discharge voltage on the size distributions of positive particles, which was conducted with a carrier gas flow rate of 5.0 L min^{-1}, capacitance of 4.4 nF, and gap distance of 0.50 mm. (b) Effects of capacitance in the circuit on the size distributions of positive particles, which was conducted with a carrier gas flow rate of 5.0 L min^{-1}, spark discharge voltage of +9.5 kV, and gap distance of 0.50 mm. (c) Effects of gap distance between two electrodes on the size distributions of positive particles, which was conducted with a carrier gas flow rate of 10.0 L min^{-1}, spark discharge voltage of +9.0 kV, and capacitance of 4.4 nF.

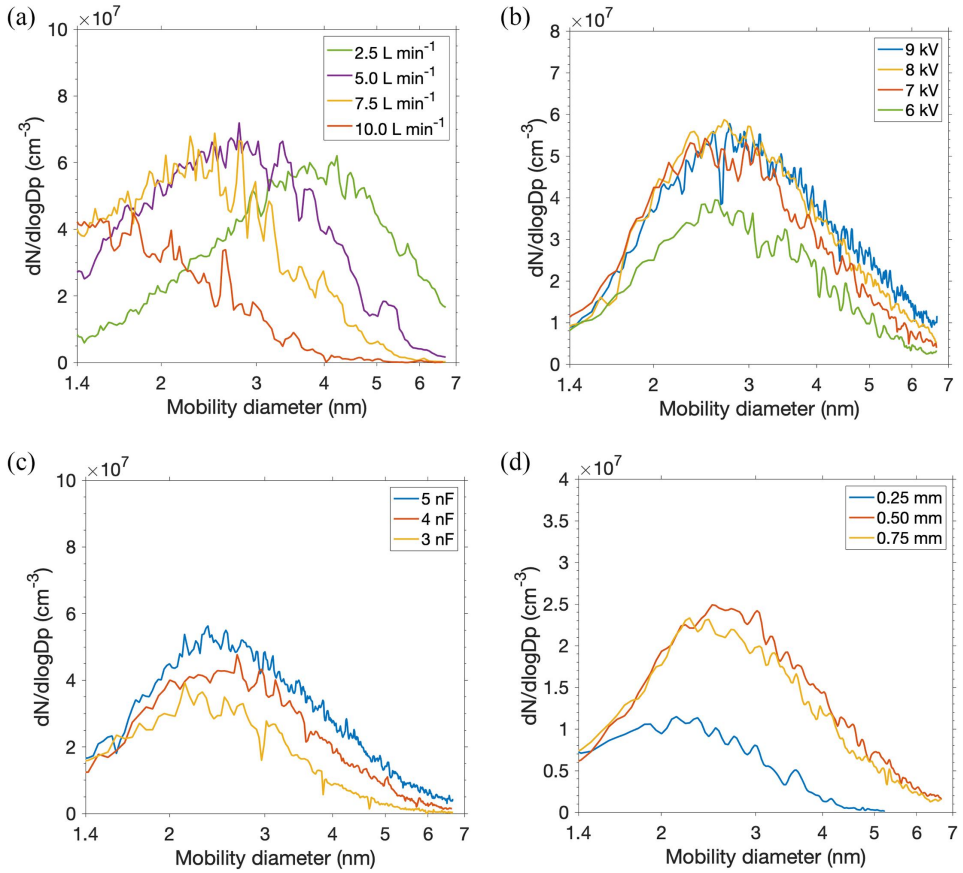

Figure 4. (a) Effects of carrier gas flow rate on the size distributions of total particles, which was conducted with a spark discharge of +9.0 kV, capacitance of 4.4 nF, and gap distance of 0.50 mm. (b) Effects of spark discharge voltage on the size distributions of total particles, which was conducted with a carrier gas flow rate of 2.5 L min^{-1}, capacitance of 4.4 nF, and gap distance of 0.50 mm. (c) Effects of capacitance in the circuit on the size distributions of total particles, which was conducted with a carrier gas flow rate of 5.0 L min^{-1}, spark discharge voltage of +9.0 kV, and gap distance of 0.50 mm. (d) Effects of gap distance between two electrodes on the size distributions of total particles, which was conducted with a carrier gas flow rate of 5.0 L min^{-1}, spark discharge voltage of +9.0 kV, and capacitance of 4.4 nF.

aligns with the results for self-charged particles. Carrier gas flow rate was the most important influencing factor for the size distribution of the produced particles. A reduction in the carrier gas flow rate resulted in an increase in particle size. The size corresponding to the peak concentration increased from sub-2 nm at 10.0 L min^{-1} to 4 nm at 2.5 L min^{-1}. Regarding the spark discharge voltage, a notable concentration increase was observed as the voltage increased from 6.0 to 7.0 kV. With the voltage further increasing from 7.0 to 9.0 kV, we observed a minor increase in particle size for particles larger than 3 nm (Figure 4b). In terms of the effects of capacitance, particle concentrations increased as capacitance increased from 3.0 to 5.0 nF (Figure 4c). Considering gap distance, both particle size and concentration increased as the gap distance expanded from 0.25 to 0.50 mm; yet a minor decrease in particle concentration was observed as the gap distance further increased to 0.75 mm (Figure 4d).

3.3. Charging properties of self-charged metal nanoparticles

3.3.1. Multiple charging conditions

Traditionally, it is expected that sub-10 nm silver particles produced by the spark discharge generator, will reach a stable state of charging, with all the particles carrying no more than a single charge. This is rooted in the abundance of bipolar plasma ions, which charge the produced particles by diffusion in a bipolarly charged environment (Wiedensohler 1988). Nevertheless, there exist additional factors that could potentially impact the charging processes. For example, the concentration and spatial distribution of bipolar ions between these electrodes remain uncertain, which might lead to potential imbalances in the charging state (Chen, McMurry, and Jiang 2018). These factors have the potential to engender the charging state of sub-10 nm Ag particles distinct from the "charging steady-state". In this section, we delve

into the charging properties of metal particles, including the multiple charging conditions and the size-resolved charge fractions.

Particles carrying multiple charges affect the accuracy of concentration measurements by the two instruments: i.e., the PSM and the AEM. If particles bear two or three charges, this correspondingly translates to a twofold or threefold alteration in particle concentrations as measured by the AEM. In contrast, the impact of multiple charges on the response of the PSM is relatively minor. The effect of particle size becomes inconsequential when the particle diameter exceeds the PSM's established cutoff size, which is typically set at ~1.5 nm (Liu et al. 2021). At this point, the detection efficiency for metal particles has already reached a plateau (Kangasluoma et al. 2015).

The concentration ratios between PSM and AEM are computed under the experimental conditions of with and without a neutralizer, as shown in Figure 5a and b, respectively. The color bar displays total counting uncertainties of PSM and AEM, which are within 30%. In the absence of a neutralizer, a shortened tube between the spark discharge generator and the half-mini DMA was utilized. Consequently, the results associated with high carrier gas flow rates represent Ag-based particles generated in the initial stage. Conversely, upon the introduction of a neutralizer, the concentration ratios of singly charged particles are presented. We further focus on the distinctions in the ratios of self-charged and singly charged particles. Only the AEM concentrations larger than 500 cm^{-3} were analyzed, to minimize the interference of background concentrations.

For singly charged particles, the concentration ratios increase from nearly 0 at 1.0 nm to a plateau value of 70%–80% at 6 nm, for both positive and

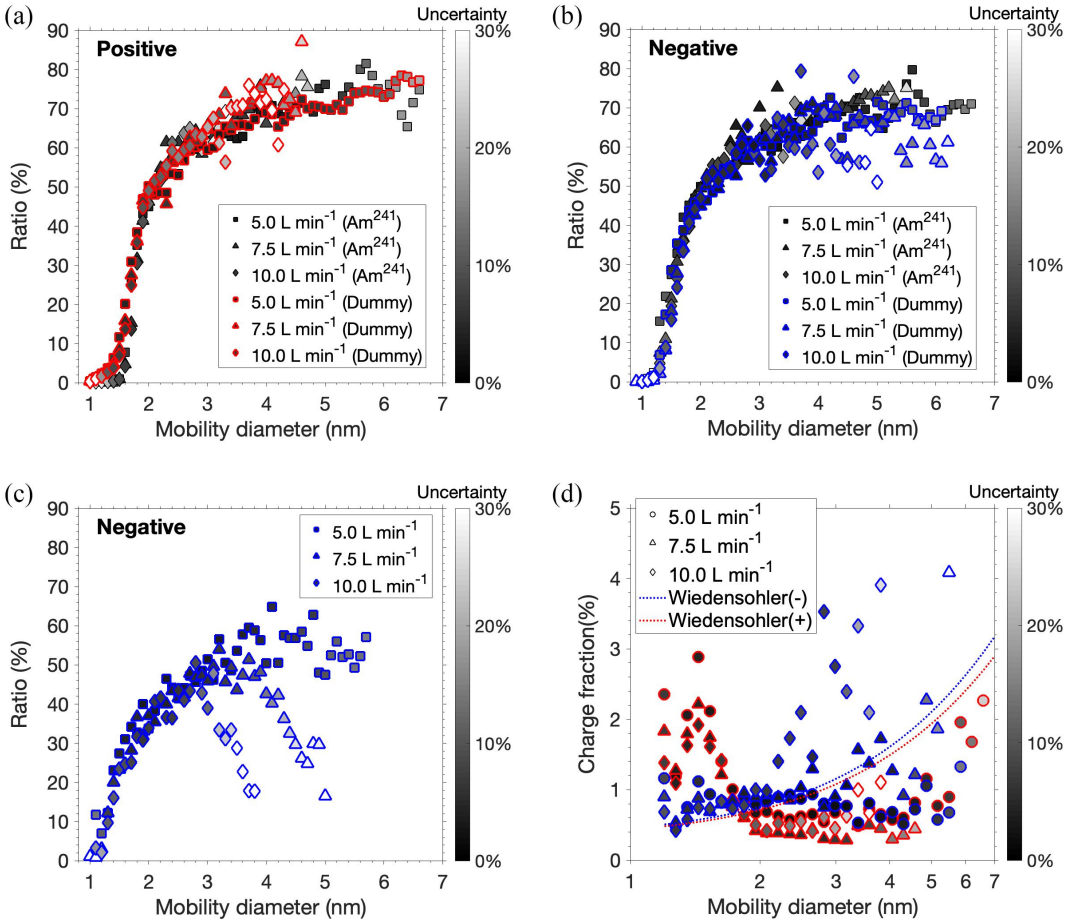

Figure 5. (a) Concentration ratios of positively charged particles measured by PSM and AEM, in the conditions of with and without the neutralizer. The non-colored symbols represent the result of singly charged particles, while the red and blue symbols represent the result of self-charged positive and negative particles. (b) Concentration ratios of negatively charged particles measured by PSM and AEM, in the condition of with and without the neutralizer. (c) Concentration ratios of positively charged particles measured by PSM and AEM under the condition of the spark discharge generator directly connected to the half-mini DMA. (d) Charge fraction of size-resolved particles. The experiments were conducted when spark discharge voltage of +9.0 kV, capacitance of 4.4 nF, and gap distance of 0.50 mm. The color bar represents the sum of counting uncertainties from PSM and AEM.

negative particles. The step rise in ratios is attributed to size-dependent detection efficiencies by PSM, associated to the Kelvin Effect (Kangasluoma and Attoui 2019; Jiang et al. 2011). For self-charged positive particles larger than 2 nm, the calculated concentration ratios closely align with those of singly charged particles. This is strong evidence that positive Ag particles carry only a single charge. The variation in carrier gas flow rate has no significant impact on the multiple charging conditions. However, a subtle difference is observed for particles smaller than 2 nm. The concentration ratios of self-charged particles show slightly higher values in comparison to those of singly charged particles. To some extent, this discrepancy stems from the fact that following the introduction of a neutralizer, the observed sub-2 nm particles include both Ag particles and neutralizer ions, which can be seen in Figure S5. Positive neutralizer ions are detected with lower efficiency by PSM when compared to the detection of metal nanoparticles, resulting in a reduction in the concentration ratios (Kangasluoma et al. 2020).

For negative particles, similar concentration ratios are evident for sub-3 nm particles between self-charged and singly charged particles (Figure 5b). Compared with the result of self-charged positive particles, the effects of negative neutralizer ions are neglectable, because the negative ions are of even smaller size, making them unlikely to impact the concentration ratios of particles larger than 1.4 nm (Figure S5). It suggests that self-charged negative particles in this size range are singly charged. Nevertheless, for particles spanning 3 to 7 nm, the ratios of self-charged particles are several percentages lower than those of singly charged particles. This trend suggests that a subset of self-charged negative particles actually possess multiple charges, which would cause the overestimation of particle concentrations by AEM. In addition, multiple charging was observed when carrier gas flow rates exceeding 7.5 L min^{-1}. However, at a carrier gas flow rate of 5.0 L min^{-1}, we did not observe the evidence of particles carrying multiple charges. The residence time might play a pivotal role in the transition from multiple charged to singly charged states. The multiple charging of negative particles should probably form at the early stage of metal particle formation. We speculate that this phenomenon occurs due to the much higher concentrations of electrons compared to positive ions within the plasma zone between the two electrodes. Consequently, particles exhibiting a strong affinity for electrons tend to carry more than one electron. However, once these particles leave the plasma zone, rapid ion-ion recombination leads to their swift neutralization by positive ions. Consequently, multiple charging is primarily observed in the case of negative particles and under conditions of high carrier gas flow rates.

To strengthen the conclusion regarding the presence of multiply charged particles, we present another set of experimental results when the spark discharge generator and the half-mini DMA were directly connected (Figure 5c and Figure S6), allowing for the measurement of multi-charging within a very short residence time. In this case, particles carrying multiple charges exhibited more pronounced characteristics. At a carrier gas flow rate of 10 L min^{-1}, we observed particles in the 3–4 nm range carrying multiple charges. At a flow rate of 7.5 L min^{-1}, particles in the 4–5 nm range were found to carry multiple charges. However, at a flow rate of 5 L min^{-1}, the features of multiple charges were less evident. This suggests that the occurrence of particles carrying multiple charges may occur in the initial stages of particle formation and that the proportion of particles carrying multiple charges gradually decreases with increasing residence time.

3.3.2. Charge fractions of self-charged particles

The size-resolved charge fractions are calculated (using Equation (5)) based on the size distributions measured with a neutralizer (negatively charged particles) and a dummy neutralizer, respectively (as depicted in Figure 5d). One need also to note, the introduction of a neutralizer or a dummy neutralizer also increased the residence time before the detection of metal particles. The charging steady state curves are plotted and used as a reference.

For both positive and negative particles, the charge fraction increases with particle size increasing from 2 to 7 nm, aligning with the predictions of diffusion charging. For positive particles, the measured charge fractions are comparable under different carrier gas flow rates. In addition, the observed charge fractions are lower than the charging steady-state curve. However, for 1.4–2.0 nm particles, the observed charge fractions are significantly higher than the charging steady-state curve, hinting that the sub-2 nm particles tend to get a positive charge. This also suggests that when we need to separate metal particles below 2 nm, not using a neutralizer can be advantageous for obtaining a higher concentration of metal-based particles.

A different trend unfolds for the charge fraction of self-charged negative particles in terms of the effects carrier gas flow rates. As the carrier gas flow rate increases, we observed an increase in charging fractions. At a carrier gas flow rate of 5.0 L min^{-1}, the

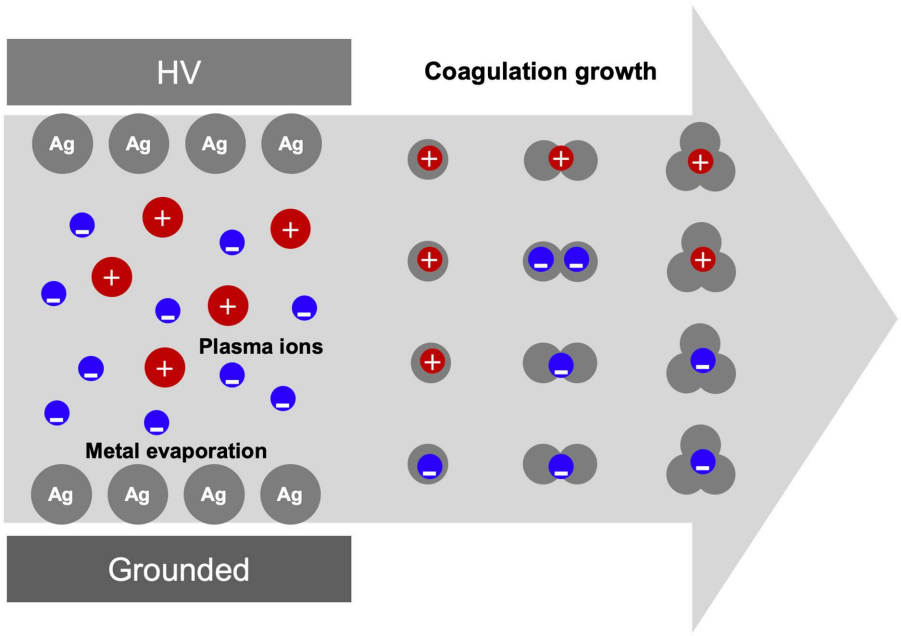

Figure 6. Schematic representation illustrating the evolution of Ag-based nanoparticles in the spark discharge generator, focusing on size distribution and charging states.

observed charge fractions are comparable to the results for positive particles. At a carrier gas flow rate of 7.5 L min^{-1}, the observed charge fractions are comparable to the charging steady-state. At a carrier gas flow rate of 10.0 L min^{-1}, particles larger than 3 nm exhibit charge fractions surpassing the charging steady state. To some extent, the increase in measured charge fraction is related to multiple charging (as displayed in Figure 5b), since some of the self-charged negative particles are multiply charged. However, as the result displayed in Figure 5b shows, the presence of multiple charging only caused a slight increase (~10%) in concentrations of AEM ($conc_{AEM}$), and fail to account for a multiple-fold increase in charge fraction under high carrier gas flow rate of 10.0 L min^{-1}.

The results regarding multiple charging and charge fractions exhibit a consistent alignment. In the presence of multiple charging, the charge fractions of negative particles exhibit a notable increase. Notably, the charge fraction of self-charged negative particles surpasses that of positive particles (as displayed in Figure 2). All these observations lead us to conclude that during the initial stages of particle formation, particles larger than 2 nm display a pronounced affinity for electrons. In contrast, particles approaching 1 nm in size tend to acquire a positive charge.

In summary, based on our measurements under different experimental conditions, the generation and growth process of sub-10 nm metal-based particles are displayed in Figure 6. Factors such as discharge voltage, electrode gap distance, and capacitance affect the concentration of metal precursors and nanoparticles concentrations, but their impact on particle size growth is less significant. Carrier gas flow rate has a pronounced effect on particle size variation and charge state. Higher carrier gas velocity corresponds to the initial generation of particles, while decreasing velocity corresponds to particle coagulation growth. In the initial stages of particle generation, positively charged particles exhibit higher charging fractions compared to negatively charged particles. Meanwhile, negatively charged particles demonstrate faster growth rates and the presence of multiple charges. With an increase in residence time and particle size, the proportion of negatively charged particles among particles larger than 3 nm increases. Further increase in residence time finally leads to convergence in the size distribution of positively and negatively charged particles, with the disappearance of multiply charged particles. At this stage, the particle size growth can be characterized using a coagulation growth model. However, for the initial generation phase, the differences in particle size distribution and charge state between positively and negatively charged particles lack theoretical or model-based explanations.

4. Conclusion

This research provides an investigation into the number size distribution and charging properties of sub-10 nm particles generated by a spark discharge generator. Effects of different factors showed comparable effects

on both the self-charged and total particles. Elevated spark discharge voltage and capacitance within the spark circuit result in heightened particle concentrations, however their effects on particle size prove to be nonsignificant. The impact of carrier gas flow rate on particle size distribution is more significant than the other parameters, with longer residence time resulting in broader distributions. Under high carrier gas flow rates, charging asymmetry between self-charged positive and negative particles are observed. Particles approximately 1 nm in size tend to favor carrying a positive charge, whereas larger particles lean toward being negatively charged, with some even exhibiting multiple charges. This observation hints the progress of Ag particle oxidation as particle size growing. On the other hand, under a carrier gas flow rate of 2.5 L min^{-1}, the charging properties of bipolar particles become comparable. This research provides insights into that how we can modify the size distribution and charging properties of metal-based particles produced in the spark discharge generator. Furthermore, it paves the way for accurate electrical mobility classification and wider application of nano-sized metal particles. The results obtained will contribute to a better comprehension of the formation mechanism of metal particles and hold significant implications for refining techniques for industrial applications.

Acknowledgment

The authors thank Hannu Koskenvaara and Jarkko Mäntylä for technical support.

Disclosure statement

No potential conflict of interest was reported by the author(s).

Funding

This study was funded by the Chongqing Natural Science Foundation (CSTB2022NSCQ-MSX1518), and the Research Council of Finland (356134, 346370, 325656).

References

Ahmed, M., and O. Kostko. 2020. From atoms to aerosols: Probing clusters and nanoparticles with synchrotron based mass spectrometry and X-ray spectroscopy. *Phys. Chem. Chem. Phys.* 22 (5):2713–37. doi: 10.1039/c9cp05802h.

Bau, S., O. Witschger, F. Gensdarmes, D. Thomas, and J.-P. Borra. 2010. Electrical properties of airborne nanoparticles produced by a commercial spark-discharge generator. *J. Nanopart. Res.* 12 (6):1989–95. doi: 10.1007/s11051-010-9856-y.

Boyen, H.-G., G. Kästle, F. Weigl, B. Koslowski, C. Dietrich, P. Ziemann, J. P. Spatz, S. Riethmüller, C. Hartmann, M. Möller, et al. 2002. Oxidation-resistant Gold-55 clusters. *Science* 297 (5586):1533–6. doi: 10.1126/science.1076248.

Cai, R., M. Attoui, J. Jiang, F. Korhonen, J. Hao, T. Petäjä, and J. Kangasluoma. 2018. Characterization of a high-resolution supercritical differential mobility analyzer at reduced flow rates. *Aerosol Sci. Technol.* 52 (11):1332–43. doi: 10.1080/02786826.2018.1520964.

Chen, X., P. H. McMurry, and J. Jiang. 2018. Stationary characteristics in bipolar diffusion charging of aerosols: Improving the performance of electrical mobility size spectrometers. *Aerosol Sci. Technol.* 52 (8):809–13. doi: 10.1080/02786826.2018.1479058.

Domaschke, M., C. Lübbert, and W. Peukert. 2019. Analysis of ultrafine metal oxide particles in aerosols using mobility-resolved time-of-flight mass spectrometry. *J. Aerosol Sci.* 137:105438. doi: 10.1016/j.jaerosci.2019.105438.

Evans, D. E., R. M. Harrison, and J. G. Ayres. 2003. The generation and characterization of metallic and mixed element aerosols for human challenge studies. *Aerosol Sci. Technol.* 37 (12):975–87. doi: 10.1080/02786820300897.

Feng, J., G. Biskos, and A. Schmidt-Ott. 2015. Toward industrial scale synthesis of ultrapure singlet nanoparticles with controllable sizes in a continuous gas-phase process. *Sci. Rep.* 5 (1):15788. doi: 10.1038/srep15788.

Fernández de la Mora, J., and J. Kozlowski. 2013. Hand-held differential mobility analyzers of high resolution for 1–30nm particles: Design and fabrication considerations. *J. Aerosol Sci.* 57:45–53. doi: 10.1016/j.jaerosci.2012.10.009.

Han, L., H. Cheng, W. Liu, H. Li, P. Ou, R. Lin, H.-T. Wang, C.-W. Pao, A. R. Head, C.-H. Wang, et al. 2022. A single-atom library for guided monometallic and concentration-complex multimetallic designs. *Nat. Mater.* 21 (6):681–8. doi: 10.1038/s41563-022-01252-y.

Isaac, N. A., M. Valenti, A. Schmidt-Ott, and G. Biskos. 2016. Characterization of tungsten oxide thin films produced by spark ablation for NO2 gas sensing. *ACS Appl. Mater. Interfaces.* 8 (6):3933–9. doi: 10.1021/acsami.5b11078.

Jiang, J., M. Chen, C. Kuang, M. Attoui, and P. H. McMurry. 2011. Electrical mobility spectrometer using a diethylene glycol condensation particle counter for measurement of aerosol size distributions down to 1 nm. *Aerosol Sci. Technol.* 45 (4):510–21. doi: 10.1080/02786826.2010.547538.

Kangasluoma, J., and M. Attoui. 2019. Review of sub-3 nm condensation particle counters, calibrations, and cluster generation methods. *Aerosol Sci. Technol.* 53 (11):1–45. doi: 10.1080/02786826.2019.1654084.

Kangasluoma, J., M. Attoui, H. Junninen, K. Lehtipalo, A. Samodurov, F. Korhonen, N. Sarnela, A. Schmidt-Ott, D. Worsnop, M. Kulmala, et al. 2015. Sizing of neutral sub 3nm tungsten oxide clusters using airmodus particle size magnifier. *J. Aerosol Sci.* 87:53–62. doi: 10.1016/j.jaerosci.2015.05.007.

Kangasluoma, J., R. Cai, J. Jiang, C. Deng, D. Stolzenburg, L. R. Ahonen, T. Chan, Y. Fu, C. Kim, T. M. Laurila, et al. 2020. Overview of measurements and current

instrumentation for 1–10 nm aerosol particle number size distributions. *J. Aerosol Sci.* 148:105584. doi: 10.1016/j.jaerosci.2020.105584.

Kangasluoma, J., and J. Kontkanen. 2017. On the sources of uncertainty in the sub-3nm particle concentration measurement. *J. Aerosol Sci.* 112:34–51. doi: 10.1016/j.jaerosci.2017.07.002.

Kim, J.-T., and J.-S. Chang. 2005. Generation of metal oxide aerosol particles by a pulsed spark discharge technique. *J. Electrost* 63 (6-10):911–6. doi: 10.1016/j.elstat.2005.03.066.

Kimble, M. L., A. W. Castleman, R. Mitrić, C. Bürgel, and V. Bonacić-Koutecký. 2004. Reactivity of atomic gold anions toward oxygen and the oxidation of CO: Experiment and theory. *J. Am. Chem. Soc.* 126 (8):2526–35. doi: 10.1021/ja030544b.

Liu, Y., M. Attoui, Y. Li, J. Chen, Q. Li, and L. Wang. 2021. Characterization of a Kanomax® fast condensation particle counter in the sub-10 nm range. *J. Aerosol Sci.* 155:105772. doi: 10.1016/j.jaerosci.2021.105772.

Luo, Z., A. W. Castleman, and S. N. Khanna. 2016. Reactivity of metal clusters. *Chem. Rev.* 116 (23):14456–92. doi: 10.1021/acs.chemrev.6b00230.

Maisser, A., K. Barmpounis, M. B. Attoui, G. Biskos, and A. Schmidt-Ott. 2015. Atomic cluster generation with an atmospheric pressure spark discharge generator. *Aerosol Sci. Technol.* 49 (10):886–94. doi: 10.1080/02786826.2015.1080812.

Maisser, A., K. Barmpounis, S. Holm, M. Attoui, A. Schmidt-Ott, J. Kangasluoma, and G. Biskos. 2021. Characterization of atmospheric-pressure spark generated atomic silver and gold clusters by time-of-flight mass spectrometry. *J. Aerosol Sci.* 156:105780. doi: 10.1016/j.jaerosci.2021.105780.

Meuller, B. O., M. E. Messing, D. L. J. Engberg, A. M. Jansson, L. I. M. Johansson, S. M. Norlén, N. Tureson, and K. Deppert. 2012. Review of spark discharge generators for production of nanoparticle aerosols. *Aerosol Sci. Technol.* 46 (11):1256–70. doi: 10.1080/02786826.2012.705448.

Morales, A. M., and C. M. Lieber. 1998. A laser ablation method for the synthesis of crystalline semiconductor nanowires. *Science* 279 (5348):208–11. doi: 10.1126/science.279.5348.208.

Petallidou, K. C., P. Ternero, M. E. Messing, A. Schmidt-Ott, and G. Biskos. 2023. Tuning atomic-scale mixing of nanoparticles produced by atmospheric-pressure spark ablation. *Nanoscale Adv.* 5 (24):6880–6. doi: 10.1039/d3na00152k.

Pfeiffer, T. V., J. Feng, and A. Schmidt-Ott. 2014. New developments in spark production of nanoparticles. *Adv. Powder Technol.* 25 (1):56–70. doi: 10.1016/j.apt.2013.12.005.

Scheibel, H. G., and J. Porstendörfer. 1983. Generation of monodisperse Ag- and NaCl-aerosols with particle diameters between 2 and 300 nm. *J. Aerosol Sci.* 14 (2):113–26. doi: 10.1016/0021-8502(83)90035-6.

Schwyn, S., E. Garwin, and A. Schmidt-Ott. 1988. Aerosol generation by spark discharge. *J. Aerosol Sci.* 19 (5):639–42. doi: 10.1016/0021-8502(88)90215-7.

Smalley, R. 1983. Laser studies of metal cluster beams. *Laser Chem.* 2 (3-4):167–84. doi: 10.1155/LC.2.167.

Spark Ablation, Building Blocks for Nanotechnology. 2019. doi: 10.1201/9780367817091.

Stolzenburg, M. R., and P. H. McMurry. 2008. Equations governing single and tandem DMA configurations and a new lognormal approximation to the transfer function. *Aerosol Sci. Technol.* 42 (6):421–32. doi: 10.1080/02786820802157823.

Tabrizi, N. S., M. Ullmann, V. A. Vons, U. Lafont, and A. Schmidt-Ott. 2008. Generation of nanoparticles by spark discharge. *J. Nanopart. Res.* 11 (2):315–32. doi: 10.1007/s11051-008-9407-y.

Ternero, P., M. Sedrpooshan, D. Wahlqvist, B. O. Meuller, M. Ek, J.-M. Hübner, R. Westerström, and M. E. Messing. 2023. Effect of the carrier gas on the structure and composition of Co–Ni bimetallic nanoparticles generated by spark ablation. *J. Aerosol Sci.* 170:106146. doi: 10.1016/j.jaerosci.2023.106146.

Vanhanen, J., J. Mikkilä, K. Lehtipalo, M. Sipilä, H. E. Manninen, E. Siivola, T. Petäjä, and M. Kulmala. 2011. Particle size magnifier for nano-CN detection. *Aerosol Sci. Technol.* 45 (4):533–42. doi: 10.1080/02786826.2010.547889.

Wiedensohler, A. 1988. An approximation of the bipolar charge distribution for particles in the submicron size range. *J. Aerosol Sci.*19 (3):387–9. doi: 10.1016/0021-8502(88)90278-9.

Wondergem, C. S., J. J. G. Kromwijk, M. Slagter, W. L. Vrijburg, E. J. M. Hensen, M. Monai, C. Vogt, and B. M. Weckhuysen. 2020. In situ shell-isolated nanoparticle-enhanced Raman spectroscopy of nickel-catalyzed hydrogenation reactions. *Chemphyschem* 21 (7):625–32. doi: 10.1002/cphc.201901162.

Zhu, Y., R. Jin, and Y. Sun. 2011. Atomically monodisperse gold nanoclusters catalysts with precise core-shell structure. *Catalysts* 1 (1):3–17. doi: 10.3390/catal1010003.